Mechanochemically assisted synthesis of La_0.7Sr_0.3MnO_3 nanoparticles and induction heating properties of the composites with hydroxyapatite

Mechanochemically assisted synthesis of $La_{0.7}Sr_{0.3}MnO_3$ nanoparticles and induction heating properties of the composites with hydroxyapatite

Tomohiro Iwasaki*, Rie Takeda

Department of Chemical Engineering, Osaka Prefecture University

1-1 Gakuen-cho, Naka-ku, Sakai, Osaka 599-8531, Japan

* Corresponding author. iwasaki@chemeng.osakafu-u.ac.jp

Abstract

Perovskite lanthanum strontium manganese oxide (LSMO, strontium-substituted lanthanum manganite) $La_{0.7}Sr_{0.3}MnO_3$ nanoparticles were synthesized via the low-temperature calcination of the precursor, which was prepared using a mechanochemical route. A powder mixture of lanthanum chloride, strontium chloride, manganese chloride and sodium carbonate was high-energy milled by a planetary ball mill under semiwet (moist) conditions to obtain the precursor. To study the mechanochemical effects on the formation of LSMO, a thermogravimetric (TG) analysis was conducted for the precursors prepared under various conditions; the precursors and the intermediates formed during calcination were identified by X-ray diffraction (XRD). The calcination of the milled precursor at 600 °C resulted in the formation of LSMO nanoparticles with good induction heating properties. The LSMO/hydroxyapatite composites exhibited rapid temperature increases in an AC magnetic field. The obtained results demonstrate that the LSMO nanoparticles and LSMO/hydroxyapatite composites are promising candidates for magnetic hyperthermia treatments.

Keywords:

Lanthanum strontium manganite; LSMO; Perovskite; Mechanochemical effect; Hydroxyapatite; Hyperthermia

1. Introduction

Strontium-substituted lanthanum manganite (lanthanum strontium manganese oxide: LSMO) is an industrially important material with perovskite structure and has been used in various functionalized materials such as magnetic thin films [1–3] and nanoparticles [4–6] because of its excellent properties [7–11]. In recent years, LSMO has attracted much interest due to good induction heating properties in alternating-current (AC) magnetic fields. Therefore, many researchers have attempted to apply LSMO nanoparticles as a heating mediator to magnetic hyperthermia treatments for cancer therapies [12–15].

Typically, LSMO nanoparticles are prepared via calcination of the precursors, i.e., solid-phase reactions of oxides, hydroxides, carbonates, nitrates, etc. of lanthanum, strontium and manganese at high temperatures [16–19]. However, considering energy saving, the calcination at low temperatures is industrially desired. For low-temperature solid-phase reactions, mechanochemical treatments of the precursors have been used prior to the calcination. In the mechanochemical methods, the precursors are subjected to high-energy ball-milling, which activates the precursors [20]. This process can increase the rate of solid-phase reactions at relatively low temperatures compared to conventional processes [21–26]. However, in many cases, the calcination at high temperatures above 750 °C is still required [21]; thus, the calcination temperature should be reduced for energy saving.

This study aims to further reduce the calcination temperature by mechanochemically preparing the precursor, which is more effective for the low-temperature synthesis of LSMO ($La_{0.7}Sr_{0.3}MnO_3$) with good induction heating properties. To determine the suitable precursor, various precursors were prepared, and the reaction temperature and formation of LSMO were analyzed. In addition, as a possible application of the synthesized LSMO nanoparticles, LSMO-incorporated biocompatible composites were studied. In this work, hydroxyapatite (denoted as HA) was used as a matrix material of the composites [27–30]. The LSMO-incorporated HA composites [31], which are expected to be heating elements for magnetic hyperthermia therapy of bone tumors, were prepared via a mechanochemical route [32,33], and their induction heating properties were investigated.

2. Experimental methods

2.1. Synthesis of LSMO nanoparticles

All reagents of analytical grade were purchased from FUJIFILM Wako Pure Chemical (Japan) and used without further purification. A planetary ball mill (P-7, Fritsch, Germany) was used to prepare the precursors of LSMO. The predetermined amounts of the starting materials, i.e., 3.5 mmol of lanthanum chloride heptahydrate ($LaCl_3 \cdot 7H_2O$), 1.5 mmol of strontium chloride hexahydrate ($SrCl_2 \cdot 6H_2O$), 5 mmol of manganese chloride tetrahydrate ($MnCl_2 \cdot 4H_2O$) and 11.8 mmol of sodium carbonate (Na_2CO_3, used as the base) were placed in the milling pot (45 mL capacity, made of silicon nitride) with 180 yttria-stabilized zirconia balls of 5 mm in diameter. A small amount (0.5 g) of deionized water was added to the pot to prevent the powders from fixing onto the pot inner wall during milling. The ball-to-powder mass ratio was approximately 18:1. The high-energy ball milling was conducted at a revolution speed of 600 rpm for 1 h (net milling time); the revolution was stopped for 5 min every 10 min of milling to avoid overheating of the powders. After the milling, the precursor, which mainly consisted of $La_2(CO_3)_3$, $SrCO_3$, $MnCO_3$ and NaCl, was obtained. The resulting precursor paste was collected from the pot and dried at 110 °C in air overnight. The dried precursor was calcined at 600 °C in air for 5 h, which formed LSMO according to the following overall reaction.

$$0.35La_2(CO_3)_3 + 0.3SrCO_3 + MnCO_3 + 0.325O_2 \rightarrow La_{0.7}Sr_{0.3}MnO_3 + 2.35CO_2 \quad (1)$$

The final product was obtained after washing the calcined powder with deionized water several time to remove NaCl, and subsequently dried at 110 °C in air overnight.

To examine the effects of the constituent of the precursor on the formation of LSMO, 23.5 mmol of sodium hydroxide (NaOH) was used as the base instead of Na_2CO_3, and the milling was performed without adding water according to the similar procedure, which provided a precursor of mainly $La(OH)_3$, $Sr(OH)_2$, $Mn(OH)_2$ and NaCl. In this case, LSMO was formed during calcination according to the following overall reaction.

$$0.7La(OH)_3 + 0.3Sr(OH)_2 + Mn(OH)_2 + 0.325O_2 \rightarrow La_{0.7}Sr_{0.3}MnO_3 + 2.35H_2O \quad (2)$$

After washing and drying, the final product was obtained.

Furthermore, to confirm the mechanochemical effects, the precursor was prepared in an aqueous solution without milling as follows. The same amounts of chlorides as those in the milling were dissolved in 10 mL of deionized water; then, 11.8 mmol of Na_2CO_3 was added to the solution to form the carbonates. The suspension was evaporated at 110 °C in air. The resulting precursor powder was calcined, washed and dried according to the described procedure. In addition, to investigate the role of NaCl in the formation of LSMO, the milled carbonate precursor was washed with deionized water to remove NaCl prior to calcination. Then, the washed precursor was dried and calcined.

2.2. Synthesis of HA nanoparticles and LSMO/HA composites

HA nanoparticles were synthesized by a mechanochemical method [34,35]. The mixture of 3 mmol of dicalcium phosphate dihydrate ($CaHPO_4 \cdot 2H_2O$) and 2 mmol of calcium carbonate ($CaCO_3$) was wet-milled in 50 mL of 1 mol/L NaOH solution for 1 h using the planetary mill at 600 rpm. The milling pot and balls were identical to those in the preparation of LSMO precursors. The molar ratio of $CaHPO_4 \cdot 2H_2O$ and $CaCO_3$ corresponded to the stoichiometric molar ratio in the formation reaction of HA expressed by Eq. (3).

$$6CaHPO_4 \cdot 2H_2O + 4CaCO_3 \rightarrow Ca_{10}(PO_4)_6(OH)_2 + 14H_2O + 4CO_2 \quad (3)$$

After milling, the formed HA nanoparticles were centrifuged and washed with deionized water several times, and dried at 60 °C in air overnight. This process can provide B-type carbonate-substituted hydroxyapatite [35]. Subsequently, the LSMO/HA composites were synthesized under dry conditions by hand-mixing the HA nanoparticles with LSMO nanoparticles for 10 min with a mortar and pestle. The LSMO nanoparticles used for this synthesis were obtained via the mechanochemical route using Na_2CO_3 without prewashing the precursor. Both the LSMO and HA nanoparticles were thoroughly washed and rinsed with deionized water after their synthesis, and the final supernatants had approximately the same level of specific conductivity as deionized water. This suggested that the LSMO and HA nanoparticles hardly contained ionic impurities that can affect the formation of the composites. The LSMO content in the composites was varied from 2 to 5 mass%.

2.3. Characterization

X-ray diffraction (XRD) analysis was conducted for the precursors and corresponding final products using a powder X-ray diffractometer (RINT-1500, Rigaku) with CuKα radiation (40 kV, 80 mA) with a wavelength of 0.154 nm. The crystallite size of LSMO of the final products was calculated using the diffraction data measured at $2\theta \approx 32.8°$, which corresponded to the (104) plane via Scherrer equation. The morphologies of the final products were observed with a field-emission scanning electron microscope (FE-SEM; JSM-6700F, JEOL) at 15 kV. To analyze the reaction processes with the degassing of CO_2 and H_2O during calcination, the thermogravimetric (TG) curve of the precursors was collected with a thermogravimetric analyzer (DTG-60, Shimadzu) at a heating rate of 10 °C/min in an air flow of 100 mL/min.

To evaluate the induction heating properties of LSMO nanoparticles, suspension samples were prepared by adding the LSMO nanoparticles (10 mass%) to glycerol [36] and ultrasonicating (50 W, 20 kHz) for 9 min to disintegrate the aggregates and disperse the particles. An AC magnetic field generator was used, which was composed of a radio frequency power source (T162-5723A, THAMWAY), an impedance matching box (T020-5723F, THAMWAY), and a solenoid coil (70-mm inner diameter) with 21 turns of water-cooled copper tube (4-mm outer diameter and 3-mm inner diameter) [36]. A glass test tube with a diameter of 15 mm was placed in the center of the coil after 2.1 g of the suspension was charged in the test tube. The temperature increase in the AC magnetic field (600 kHz, 5 kA/m) was measured with an optical fiber thermometer (FTI-10 with FOT-L-NS-967, FISO Technologies). In the evaluation for the LSMO/HA composites, 0.4 g of the composite powder was placed in the glass tube under dry conditions without glycerol and closely packed by tapping the tube. The temperature was measured according to the described method for LSMO particles.

In addition, a release test of heavy metals was performed in a physiological saline solution to examine the safety of the LSMO/HA composites in hyperthermia applications. Briefly, 0.1 g of the LSMO nanoparticles used for the synthesis of the composites were soaked in 50 mL of 0.9 w/v% NaCl solution at 43 °C for 24 h under stirring. The elemental analysis by energy

dispersive X-ray spectroscopy (EDX; Epsilon 1, Malvern Panalytical) was performed to check the elution of the heavy metals.

3. Results and discussion

3.1. Synthesis of LSMO

Figure 1 shows the TG curves of the precursors mechanochemically prepared using Na_2CO_3 and NaOH. The mass of the precursor composed of the carbonates decreased at 3 temperature levels of approximately 279, 418 and 571 °C. In contrast, the hydroxide precursor had a clear mass reduction only at approximately 591 °C. Although this temperature was higher than that (571 °C) of the third mass reduction in the carbonate precursor, the results suggest that the calcination of the precursors at 600 °C results in the formation of LSMO in both cases. Figure 2 shows the XRD patterns of the precursors and corresponding final products. The carbonate precursor contained $La_2O(CO_3)_2 \cdot xH_2O$ as the carbonate of lanthanum. The hydroxide precursor consisted of $La(OH)_3$ and $SrCO_3$, which could be derived from $Sr(OH)_2$ and CO_2 in air. In both precursors, no clear diffraction peaks of carbonates of strontium and/or manganese were observed, which may be due to the amorphization. The XRD analysis of the final products confirms the formation of the perovskite-structured LSMO phase (JCPDS No. 51-0409) from both precursors. The crystallite size of the LSMO nanoparticles from the carbonate precursor was determined to 15.6 nm, which was slightly larger than that (14.9 nm) from the hydroxide precursor. The reason may be that the carbonate precursor started to react at relatively low temperatures, which prolonged the crystal growth period during the calcination. Figure 3 depicts the SEM images of the final products observed at ×40,000 magnification. The particle sizes were almost identical (approximately 50–100 nm); however, the final product from the hydroxide precursor slightly contained a needle-like phase as impurities, probably $La(OH)_2$ and/or La_2O_3 (Fig. 2d) [37,38], which suggests that the formation reactions were unfinished during the calcination. Figure 4 shows the temperature increase in the AC magnetic field. The temperature of the final product from the carbonate precursor rapidly increased with time, which indicates that it has good induction heating properties. This may be due to the larger

crystallite size and higher purity of LSMO. The obtained results reveal that the carbonate precursor, i.e., the use of Na_2CO_3 as the base, was effective for the synthesis of LSMO nanoparticles using this process.

3.2. Formation process of LSMO during calcination

Based on the TG curve of the carbonate precursor in Fig. 1a, the samples prepared by the calcination of the precursor at 350 °C and 500 °C for 1 h, followed by washing, were analyzed by XRD. According to Figs. 2a and 5a, there were no remarkable differences except for the NaCl removal, which implies that the dehydration of $La_2O(CO_3)_2 \cdot xH_2O$ (i.e., reduction of x) may mainly occur at the first mass reduction step (i.e., at approximately 280 °C) [39]. Figures 1a and 5b confirm that in the second step at approximately 420 °C, LSMO was formed. In general, for example, the formation of $La_2O_2CO_3$ from $La_2O(CO_3)_2 \cdot xH_2O$ and the formation of La_2O_3 by the decarboxylation of $La_2O_2CO_3$ can occur at temperatures above 400 °C and 700 °C, respectively [39]. Therefore, the results demonstrate that the mechanochemical preparation of the carbonate precursor can effectively contribute to the formation reactions of LSMO at low temperatures.

Figures 6 and 7 show the TG curve of the carbonate precursor prepared without milling and the XRD patterns of the precursor before and after the calcination, respectively. The mass reduction was observed in 3 steps at 317, 427 and 633 °C (Fig. 6), which was a similar tendency to the case of the milled precursor in Fig. 1a. However, the temperatures were higher than those of the milled precursor. According to Figs. 2c and 7a, the unmilled precursor had a similar composition to the milled precursor; however, the calcination of the unmilled precursor could not finish the formation reactions, as shown in Fig. 7b, which resulted in a low yield of LSMO and formation of byproducts such as LaOCl. Therefore, the milling of the precursor can increase its reactivity by the mechanochemical activation, which may enhance the reaction rate at low temperatures.

The TG curve of the washed carbonate precursor and the XRD patterns of the precursor before and after the calcination are shown in Figs. 8 and 9, respectively. Although the precursor

underwent the mechanochemical treatment, it needed higher temperatures for the reactions (Fig. 8), which resulted in incomplete formation reactions of LSMO during the calcination at 600 °C (Fig. 9). By washing, NaCl was removed from the precursor. Accordingly, it is suggested that NaCl in the precursor plays an important role in a rapid progress of the reactions, although NaCl is not a reactive component in the formation reactions. In addition, the washing can reduce the surface energy of the mechanochemically activated reactant particles by wetting, which decreases the activation of the precursor and may increase the reaction temperatures.

3.3. Induction heating properties of LSMO/HA composites

Figure 10 shows the XRD pattern and SEM image (magnification: ×30,000) of 5 mass% LSMO/HA composite as an example, which confirms that the LSMO nanoparticles were well distributed in the HA matrix. The HA peaks in the XRD pattern (Fig. 10a) almost coincided with those in a typical XRD pattern of carbonate hydroxyapatite [40]. Figure 11 depicts the temperature profiles of LSMO/HA composites with various LSMO contents in the AC magnetic field. Rapid temperature increases were observed, which implies that the LSMO/HA composites had good hyperthermia properties even at low LSMO contents. Furthermore, using the 5-mass% LSMO/HA composite, we attempted to control the temperature (Fig. 12). The temperature was adjusted to 37 °C, which was a normal human body temperature, before subjected to the AC magnetic field. By induction heating, the temperature was quickly increased and successfully controlled at approximately 43±1 °C by a simple on-off control of the AC magnetic field. The EDX analysis of the supernatant after the release test for the LSMO nanoparticles demonstrated no elution of the heavy metals, implying the non-toxicity of the LSMO/HA composites. The obtained results suggest that the LSMO/HA composites may be promising candidates as a heating mediator for magnetic hyperthermia therapy of bone tumors.

4. Conclusions

The LSMO nanoparticles with good induction heating properties were synthesized by the calcination of a special precursor at 600 °C, which was a relatively low temperature compared

to those in conventional processes. The formation of LSMO was analyzed through the TG and XRD analyses of various precursors, intermediates and final products, which demonstrates that the precursor mechanochemically prepared by ball-milling the carbonates of La, Sr and Mn was effective for the low-temperature synthesis. Furthermore, the LSMO/HA composites were synthesized by simply mixing the LSMO and HA powders and exhibited good induction heating properties, which suggests that the composites are promising candidates for magnetic hyperthermia therapy of bone tumors.

Acknowledgement

This study was financially supported in part by JSPS KAKENHI Grant Number JP19K05216.

References

[1] S. Kumari, N. Mottaghi, C.-Y. Huang, R. Trappen, G. Bhandari, S. Yousefi, G. Cabrera, M.S. Seehra, M.B. Holcomb, Effects of oxygen modification on the structural and magnetic properties of highly epitaxial $La_{0.7}Sr_{0.3}MnO_3$ (LSMO) thin films, Sci. Rep. 10 (2020) 3659. https://doi.org/10.1038/s41598-020-60343-5.

[2] M.C. Ramírez Camacho, C.F. Sánchez Valdés, M. Curiel, J.L. Sánchez Llamazares, J.M. Siqueiros, O. Raymond Herrera, Superparamagnetic state in $La_{0.7}Sr_{0.3}MnO_3$ thin films obtained by rf-sputtering, Sci. Rep. 10 (2020) 2568. https://doi.org/10.1038/s41598-020-59334-3.

[3] T. Bolstad, E. Lysne, U.L. Österberg, T. Tybell, Thickness dependent uniaxial magnetic anisotropy due to step-edges in (1 1 1)-oriented $La_{0.7}Sr_{0.3}MnO_3$ thin films, J. Magn. Magn. Mater. 487 (2019) 165304. https://doi.org/10.1016/j.jmmm.2019.165304.

[4] D. Deb, S.K. Mandal, A. Lakhani, A. Nath, P. Dey, Interface driven electrical and magneto-transport properties of $(100–x)\%$ $La_{0.7}Sr_{0.3}MnO_3$–$x\%$ Paraffin wax ($0 \leq x \leq 1$) hybrid nanocomposites, Eur. Phys. J. B 92 (2019) 165. https://doi.org/10.1140/epjb/e2019-100169-5.

[5] R. Debnath, S.K. Mandal, A. Nath, Inorganic-organic hybrid nanocomposites:

magnetoelectric coupling, dielectric and AC electrical response, Mater. Lett. 237 (2019) 80–82. https://doi.org/10.1016/j.matlet.2018.11.077.

[6] C. Chen, W. Zhang, S. Zhu, C. Cai, Abnormal transport and magnetic properties induced by change of the phase volume ratio for $YBa_2Cu_3O_{7-\delta}/La_{0.67}Sr_{0.33}MnO_3$ hybrids, J. Supercond. Nov. Magn. 31 (2018) 2019–2025. https://doi.org/10.1007/s10948-017-4470-1.

[7] G. Kandasamy, Recent advancements in manganite perovskites and spinel ferrite-based magnetic nanoparticles for biomedical theranostic applications, Nanotechnology 30 (2019) 502001. https://doi.org/10.1088/1361-6528/ab3f17.

[8] Z. Liao, J. Zhang, Metal-to-insulator transition in ultrathin manganite heterostructures, Appl. Sci. 9 (2019) 144. https://doi.org/10.3390/app9010144.

[9] S. Majumdar, S.V. Dijken, Pulsed laser deposition of $La_{1-x}Sr_xMnO_3$: thin-film properties and spintronic applications, J. Phys. D 47 (2014) 034010. https://doi.org/10.1088/0022-3727/47/3/034010.

[10] J. Jiang, Q.-M. Chen, X. Liu, First-principles study on the electronic structure and optical properties of $La_{0.75}Sr_{0.25}MnO_{3-\sigma}$ materials with oxygen vacancies defects, Curr. Appl. Phys. 18 (2018) 200–208. https://doi.org/10.1016/j.cap.2017.12.005.

[11] I.W. Seo, Y.S. Lee, J.W. Seo, S.-H. Baek, Optical investigation of the metal-insulator transition in the manganite films with the thickness dependence, Curr. Appl. Phys. 19 (2019) 1019–1023. https://doi.org/10.1016/j.cap.2019.06.002.

[12] A.S. Khan, N. Mehboob, M.F. Nasir, A. Hamayun, Magnetic and heating aptitudes of PEG coated $La_{0.73}Sr_{0.27}MnO_3$ and $La_{0.67}Sr_{0.33}MnO_3$ mediators towards hyperthermia methodology, Physica B 564 (2019) 125–132. https://doi.org/10.1016/j.physb.2019.03.039.

[13] R. Kumar, A. Chauhan, S.K. Jha, B.K. Kuanr, Encapsulated lanthanum strontium manganese oxide in mesoporous silica shell: potential for cancer treatment by hyperthermia therapy, J. Alloy. Compd. 790 (2019) 433–446. https://doi.org/10.1016/j.jallcom.2019.03.163.

[14] S. Lotfi, S. Bahari, A. Bahari, M. Roudbari, Magnetic performance and evaluation of radiofrequency hyperthermia of perovskite $La_{1-x}Sr_xMnO_3$, J. Supercond. Nov. Magn. 31 (2018) 2187–2193. https://doi.org/10.1007/S10948-017-4475-9.

[15] H. Das, A. Inukai, N. Debnath, T. Kawaguchi, N. Sakamoto, S.M. Hoque, H. Aono, K. Shinozaki, H. Suzuki, N. Wakiya, Influence of crystallite size on the magnetic and heat generation properties of $La_{0.77}Sr_{0.23}MnO_3$ nanoparticles for hyperthermia applications, J. Phys. Chem. Solids 112 (2018) 179–184. https://doi.org/10.1016/j.jpcs.2017.09.030.

[16] K. Navin, R. Kurchania, A comparative study of the structural, magnetic transport and electrochemical properties of $La_{0.7}Sr_{0.3}MnO_3$ synthesized by different chemical routes, Appl. Phys. A 126 (2020) 100. https://doi.org/10.1007/s00339-019-3269-2.

[17] R.T. Salakhova, A.P. Pyatakov, V.I. Zverev, B. Pimentel, R.J.C. Vivas, L.A. Makarova, N.S. Perov, A.M. Tishin, A.A. Shtil, M.S. Reis, The frequency dependence of magnetic heating for $La_{0.75}Sr_{0.25}MnO_3$ nanoparticles, J. Magn. Magn, Mater. 470 (2019) 38–40. https://doi.org/10.1016/j.jmmm.2017.11.126.

[18] K. Navin, R. Kurchania, The effect of particle size on structural, magnetic and transport properties of $La_{0.7}Sr_{0.3}MnO_3$ nanoparticles, Ceram. Int. 44 (2018) 4973–4980. https://doi.org/10.1016/j.ceramint.2017.12.091.

[19] P.K. Yap, A.H. Shaari, H. Baqiah, C.S. Kien, J. Hassan, M.M.A. Kechik, L.K. Pah, Z.A. Talib, Growth and magnetic behaviours of $La_{0.7}Sr_{0.3}MnO_3$ nanoparticles synthesized via thermal treatment method, Sains Malays. 48 (2019) 369–375. http://dx.doi.org/10.17576/jsm-2019-4802-14.

[20] E. Skwarek, S. Khalameida, W. Janusz, V. Sydorchuk, N. Konovalova, V. Zazhigalov, J. Skubiszewska-Zięba, R. Leboda, Influence of mechanochemical activation on structure and some properties of mixed vanadium-molybdenum oxides, J. Therm. Anal. Calorim. 106 (2011) 881–894. https://doi.org/10.1007/s10973-011-1744-x.

[21] J.-L. Ortiz-Quiñonez, L. García-González, F.E. Cancino-Gordillo, U. Pal, Particle dispersion and lattice distortion induced magnetic behavior of $La_{1-x}Sr_xMnO_3$ perovskite nanoparticles grown by salt-assisted solid-state synthesis, Mater. Chem. Phys. 246 (2020) 122834. https://doi.org/10.1016/j.matchemphys.2020.122834.

[22] M.A.A. Bally, F.A. Khan, Structural, dielectric and magnetic properties of $La_{0.55}Sr_{0.45}MnO_3$ polycrystalline perovskite, J. Magn. Magn. Mater. 509 (2020) 166897.

https://doi.org/10.1016/j.jmmm.2020.166897.

[23] A.M. Bolarín-Miró, C.A. Taboada-Moreno, C.A. Cortés-Escobedo, O. Rosales-González, G. Torres-Villaseñor, F. Sánchez-De Jesús, Effect of high-energy ball milling on the magnetocaloric properties of $La_{0.7}Ca_{0.2}Sr_{0.1}MnO_3$, Appl. Phys. A 126 (2020) 369. https://doi.org/10.1007/s00339-020-03555-w.

[24] C.A. Taboada-Moreno, F. Sánchez-De Jesús, F. Pedro-García, C.A. Cortés-Escobedo, J.A. Betancourt-Cantera, M. Ramírez-Cardona, A.M. Bolarín-Miró, Large magnetocaloric effect near to room temperature in Sr doped $La_{0.7}Ca_{0.3}MnO_3$, J. Magn. Magn. Mater. 496 (2020) 165887. https://doi.org/10.1016/j.jmmm.2019.165887.

[25] M.E. Botello-Zubiate, M.C. Grijalva-Castillo, D. Soto-Parra, R.J. Sáenz-Hernández, C.R. Santillán-Rodríguez, J.A. Matutes-Aquino, Preparation of $La_{0.7}Ca_{0.3-x}Sr_xMnO_3$ manganites by four synthesis methods and their influence on the magnetic properties and relative cooling power, Materials 12 (2019) 309. https://doi.org/10.3390/ma12020309.

[26] A.D. Souza, P.D. Babu, S. Rayaprol, M.S. Murari, L.D. Mendonca, M. Daivajna, Size control on the magnetism of $La_{0.7}Sr_{0.3}MnO_3$, J. Alloy. Compd. 797 (2019) 874–882. https://doi.org/10.1016/j.jallcom.2019.05.004.

[27] Y. Liu, M. Wang, Developing a composite material for bone tissue repair, Curr. Appl. Phys. 7 (2007) 547–554. https://doi.org/10.1016/j.cap.2006.11.002.

[28] G. Xiong, Y. Wan, G. Zuo, K. Ren, H. Luo, Self-assembled magnetic lamellar hydroxyapatite as an efficient nano-vector for gene delivery, Curr. Appl. Phys. 15 (2015) 811–818. https://doi.org/10.1016/j.cap.2015.04.032.

[29] T.G.M. Bonadio, V.F. Freitas, T.T. Tominaga, R.Y. Miyahara, J.M. Rosso, L.F. Cótica, M.L. Baesso, W.R. Weinand, I.A. Santos, R. Guo, A.S. Bhalla, Polyvinylidene fluoride/hydroxyapatite/β-tricalcium phosphate multifunctional biocomposite: potentialities for bone tissue engineering, Curr. Appl. Phys. 17 (2017) 767–773. https://doi.org/10.1016/j.cap.2017.02.022.

[30] E. Broda, E. Skwarek, V.V. Payentko, V.M. Gunko, Synthesis and selected physicochemical properties of hydroxyapatite and white clay composite, Physicochem. Probl.

Miner. Process. 55 (2019) 1475–1483. https://doi.org/10.5277/ppmp19073.

[31] S. Keshri, V. Kumar, P. Wiśniewski, A.S. Kamzin, Synthesis and characterization of LSMO manganite-based biocomposite, Phase Transit. 87 (2014) 468–476. https://doi.org/10.1080/01411594.2013.869331.

[32] B. Charmas, J. Skubiszewska-Zięba, K. Kucio, E. Skwarek, Influence of mechanochemical treatment on thermal and structural properties of silica-collagen and hydroxyapatite-collagen composites, Adsorption 25 (2019) 591–599. https://doi.org/10.1007/s10450-019-00051-3.

[33] M. Ramli, F. Rahmawati, Febriani, Saiful, N. Idris, Synthesis of magnetic inorganic-catalyst prepared from Aceh's bovine bone waste by mechanochemical method, AIP Conf. Proc. 2243 (2020) 020021. https://doi.org/10.1063/5.0001114.

[34] A. Ruksudjarit, K. Pengpat, G. Rujijanagul, T. Tunkasiri, Synthesis and characterization of nanocrystalline hydroxyapatite from natural bovine bone, Curr. Appl. Phys. 8 (2008) 270–272. https://doi.org/10.1016/j.cap.2007.10.076.

[35] T. Iwasaki, R. Nakatsuka, K. Murase, H. Takata, H. Nakamura, S. Watano, Simple and rapid synthesis of magnetite/hydroxyapatite composites for hyperthermia treatments via a mechanochemical route, Int. J. Mol. Sci. 14 (2013) 9365–9378. https://doi.org/10.3390/ijms14059365.

[36] F. Hirosawa, T. Iwasaki, S. Watano, Synthesis and magnetic induction heating properties of Gd-substituted Mg–Zn ferrite nanoparticles, Appl. Nanosci. 7 (2017) 209–214. https://doi.org/10.1007/s13204-017-0566-y.

[37] G. Li, C. Li, Z. Xu, Z. Cheng, J. Lin, Facile synthesis, growth mechanism and luminescence properties of uniform $La(OH)_3$: Ho^{3+}/Yb^{3+} and La_2O_3 : Ho^{3+}/Yb^{3+} nanorods, CrystEngComm 12 (2010) 4208–4216. https://doi.org/10.1039/C0CE00075B.

[38] X. Xiao, Y. Huang, F. Dong, Synthesis and application of one-dimensional $La(OH)_3$ nanostructures: an overview, J. Chem. 2014 (2014) 305986. https://doi.org/10.1155/2014/305986.

[39] Y. Gao, Y. Masuda, K. Koumoto, Micropatterning of lanthanum-based oxide thin film on

self-assembled monolayers, J. Colloid Interface Sci. 274 (2004) 392–397. https://doi.org/10.1016/j.jcis.2004.02.050.

[40] J.J. Lovón-Quintana, J.K. Rodriguez-Guerrero, P.G. Valença, Carbonate hydroxyapatite as a catalyst for ethanol conversion to hydrocarbon fuels, Appl. Catal. A 542 (2017) 136–145. https://doi.org/10.1016/j.apcata.2017.05.020.

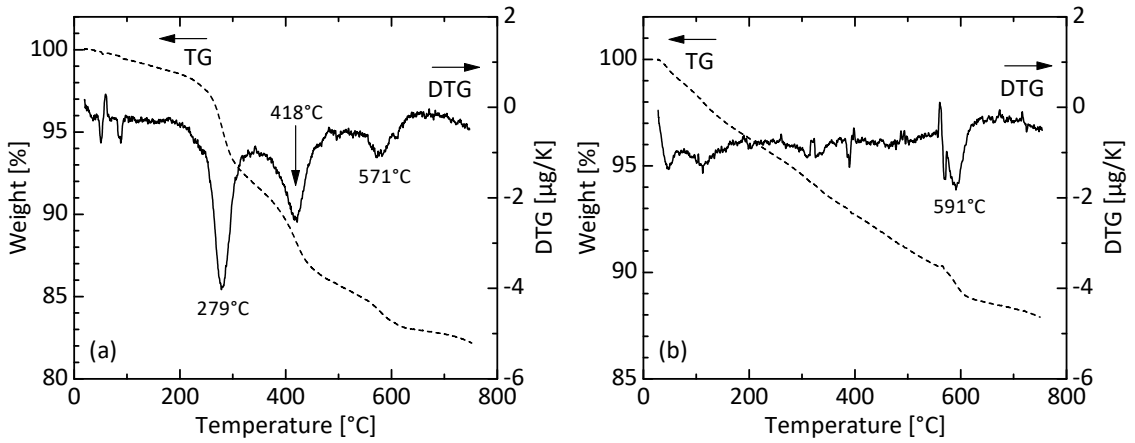

Fig. 1. TG and DTG curves of the precursors mechanochemically prepared using (a) Na_2CO_3 and (b) NaOH.

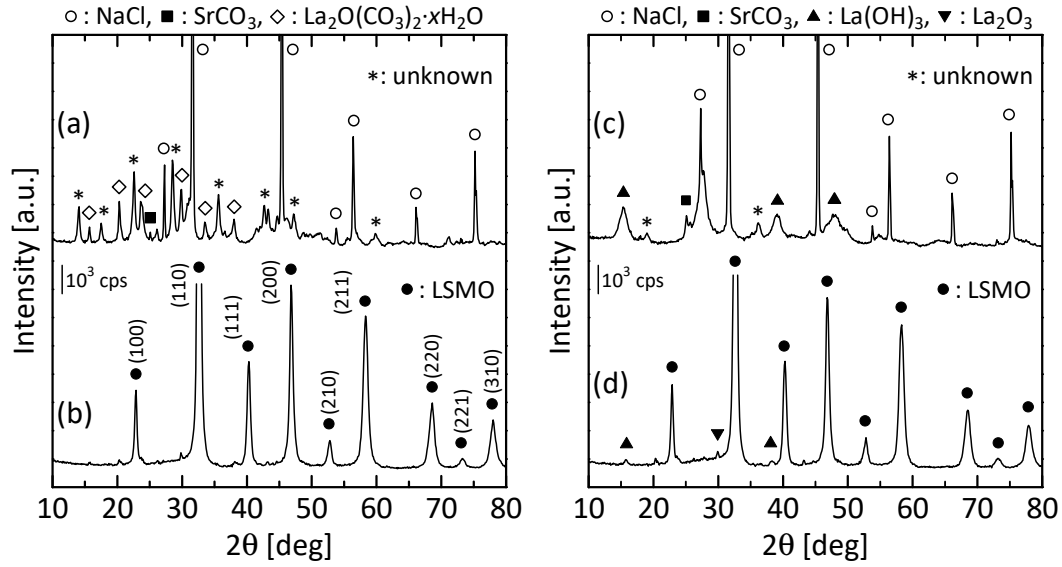

Fig. 2. XRD patterns of the (a, c) mechanochemically prepared precursors and (b, d) corresponding final products using (a, b) Na_2CO_3 and (c, d) NaOH.

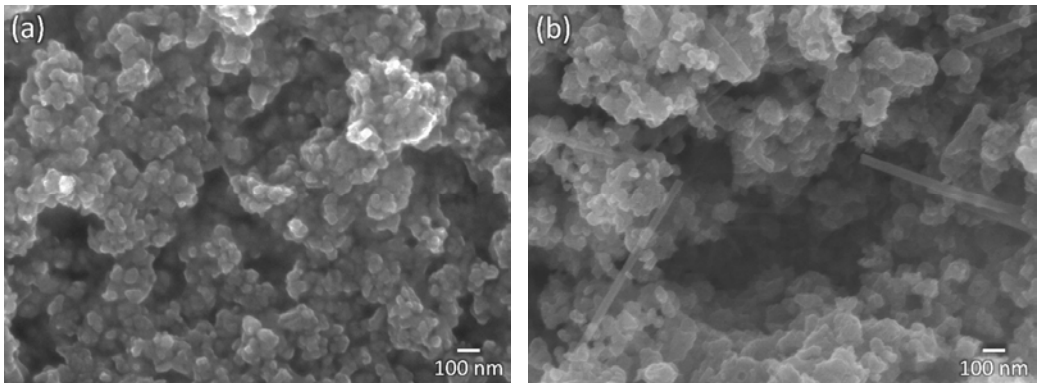

Fig. 3. SEM images of the final products obtained from the (a) carbonate and (b) hydroxide precursors.

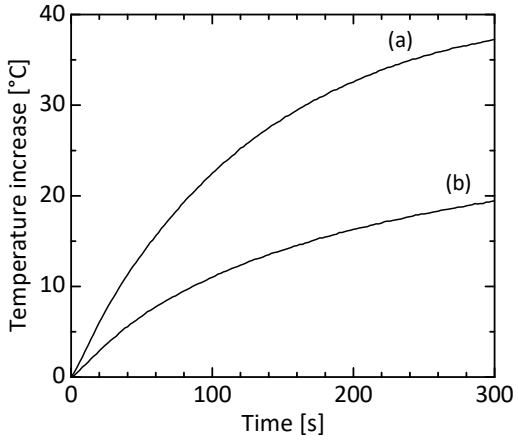

Fig. 4. Temperature profiles of the final products obtained from the (a) carbonate and (b) hydroxide precursors in the AC magnetic field.

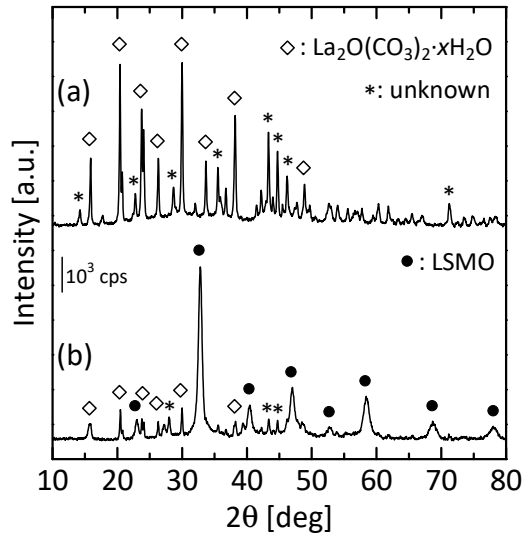

Fig. 5. XRD patterns of the samples prepared by the calcination of the carbonate precursor at (a) 350 °C and (b) 500 °C for 1 h.

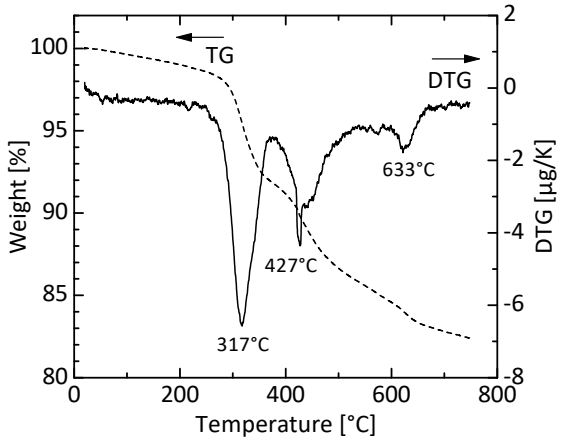

Fig. 6. TG curve of the carbonate precursor prepared in an aqueous solution without milling.

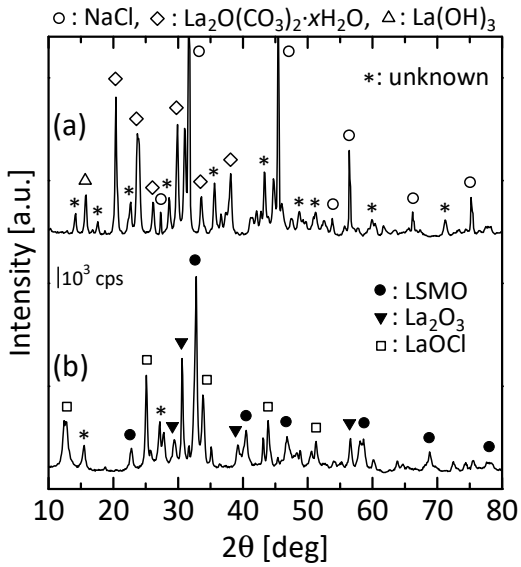

Fig. 7. XRD patterns of the unmilled carbonate precursor (a) before and (b) after calcination.

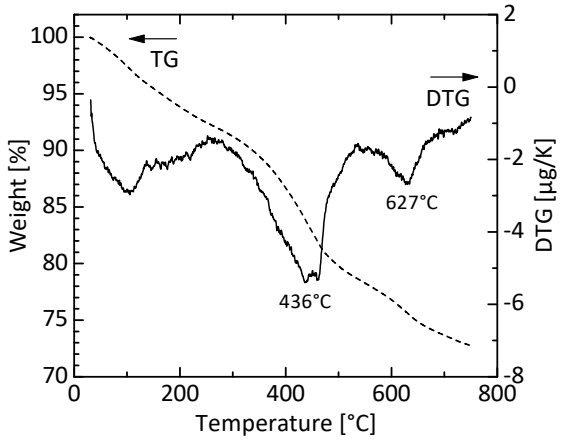

Fig. 8. TG curve of the washed precursor.

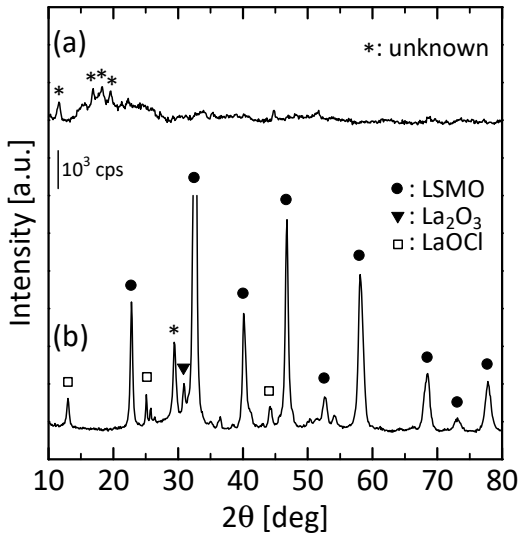

Fig. 9. XRD patterns of the washed precursor (a) before and (b) after calcination.

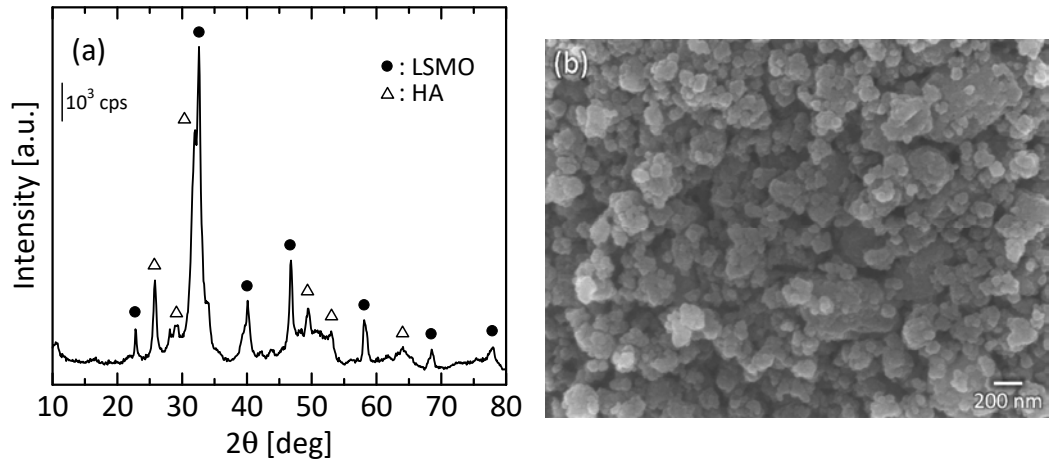

Fig. 10. (a) XRD pattern and (b) SEM image of the 5-mass% LSMO/HA composite.

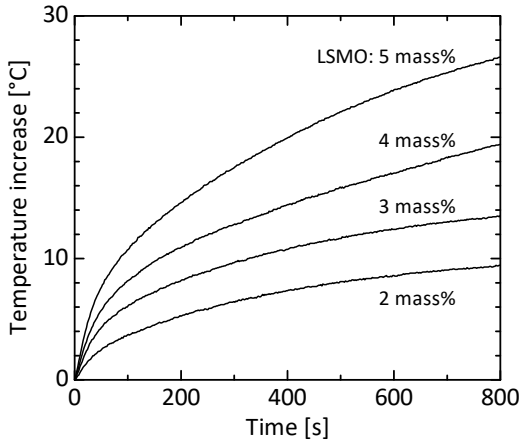

Fig. 11. Temperature profiles of LSMO/HA composites with various LSMO contents in the AC magnetic field.

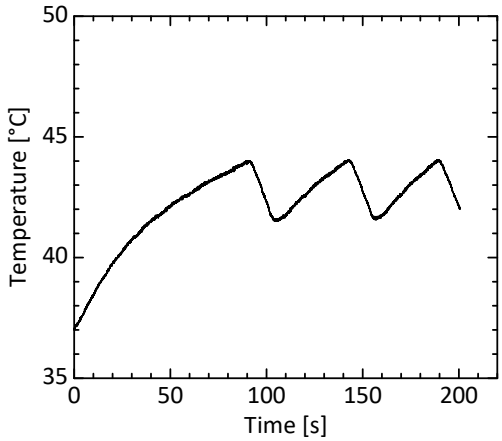

Fig. 12. Temperature control of 5-mass% LSMO/HA composites by the on-off control of the AC magnetic field.